

DOI- and TOF-capable PET array detector using double-ended light readout and stripline-based row and column electronic readout

Fei Wang ¹, Chien-Min Kao ², Yuexuan Hua ², Linfeng Liu ², Xiaoyu Zhang ², Heejong Kim ², Woon-Seng Choong ², and Qingguo Xie ²

¹the College of Life Science and Technology

²Affiliation not available

October 31, 2023

Abstract

We investigate an economic readout for depth-of-interaction (DOI) and time-of-flight capable PET detector that consists of an $N \times N$ array of crystals whose light outputs at the front- and back-end surfaces are detected by using silicon photomultipliers (SiPM). The $N \times N$ SiPMs at the front-end (back-end) of the detector are read by a stripline configured to support discrimination of the row (column) position of the signal-producing crystal, producing only four outputs for the detector. To evaluate this design, we built 4×4 and 8×8 detector modules (DM) by using $3.0 \times 3.0 \times 20$ mm³ lutetium-yttrium oxyorthosilicates. The outputs were sampled at 2 GHz and processed offline. For both DMs, crystal discrimination was successful. For the 4×4 (8×8) DM, we obtained a crystal-level energy resolution ranging from 11.3% to 19.3% with an average of 14.1% (9.5% to 21.6% with an average of 13.9%), an average DOI resolution of 2.5 mm (3.1 mm), and a best coincidence resolving time (CRT), measured in coincidence with a single-pixel reference detector with a 302 ps CRT, of 391 ps (603 ps). The CRT deteriorated with the (8×8) DM possibly due to intercrystal scattering.

DOI- and TOF-capable PET array detector using double-ended light readout and stripline-based row and column electronic readout

Fei Wang, Chien-Min Kao, Xiaoyu Zhang, Linfeng Liu, Yuexuan Hua, Heejong Kim, Woon-Seng Choong, and Qingguo Xie*

Abstract—We investigate an economic readout for depth-of-interaction (DOI) and time-of-flight capable PET detector that consists of an $N \times N$ array of crystals whose light outputs at the front- and back-end surfaces are detected by using silicon photomultipliers (SiPM). The $N \times N$ SiPMs at the front-end (back-end) of the detector are read by a stripline configured to support discrimination of the row (column) position of the signal-producing crystal, producing only four outputs for the detector. To evaluate this design, we built 4×4 and 8×8 detector modules (DM) by using $3.0 \times 3.0 \times 20$ mm³ lutetium-yttrium oxyorthosilicates. The outputs were sampled at 2 GHz and processed offline. For both DMs, crystal discrimination was successful. For the 4×4 (8×8) DM, we obtained a crystal-level energy resolution ranging from 11.3% to 19.3% with an average of 14.1% (9.5% to 21.6% with an average of 13.9%), an average DOI resolution of 2.5 mm (3.1 mm), and a best coincidence resolving time (CRT), measured in coincidence with a single-pixel reference detector with a 302 ps CRT, of 391 ps (603 ps). The CRT deteriorated with the (8×8) DM possibly due to intercrystal scattering.

Index Terms—PET detector, depth-of-interaction, time-of-flight, multiplexing, stripline.

I. INTRODUCTION

PET detector is a critical component of a PET system such that it determines the performance properties of the system. The ideal PET detector is one that can lead to a system having simultaneously high resolution and high sensitivity while allowing effective rejection of scattered and random events [1]–[3]. The advents of silicon photomultiplier (SiPM), which is a compact and high-gain solid-state photosensor, and scintillators such as lutetium-yttrium oxyorthosilicate (LYSO) that are dense, bright, and fast have enabled the development of PET detectors of this kind. SiPM is available from 1 to

5 mm in size. For high-resolution clinical imaging, 2-3 mm width LYSO crystals and SiPMs are often used [4], [5]. To provide adequate detection efficiency for 511 keV photons, 20 mm or longer LYSO crystals are needed. Time-of-flight (TOF) imaging also can lead to a gain in the statistics of the resulting image, hence increasing the effective sensitivity of a system. To first order, the gain is inversely proportional to the coincidence resolving time (CRT). Using SiPMs and fast electronics, sub 100 ps CRT has been reported for 3-5 mm length LYSO-type scintillators [6]. When 20 mm length scintillators are used, the CRT degrades but still can reach 240-400 ps [7]–[12]. Longer crystals also lead to DOI blurring that degrades the transverse image resolution at positions away from the center of the system. For long axial field-of-view (FOV) systems, DOI blurring limits the axial image resolution for all positions. The issues due to DOI blurring can be addressed if the detector provides DOI measurement. The compactness of SiPM has enabled many DOI-capable detector designs, including double-ended light readout [13], side readout [14], [15], and multi-layered configurations [16]. DOI measurement, which effectively partitions a long scintillator into multiple shorter segments, can also be used to improve CRT [17], [18].

However, the development of high-efficiency and high-resolution PET array detectors capable of superior DOI and TOF resolutions is challenging due to the issue of complexity. For example, for improving resolution the state-of-the-art clinical PET systems uses scintillators that are approximately 3×3 mm² in cross-section [19]–[22]. A 5×5 cm² detector therefore can have 16×16 (256) crystals. When using the double-ended light readout to produce DOI measurement, such a detector has 512 SiPMs. A 20-cm length, 80-cm diameter PET system can employ 200 such detectors and more than 100,000 SiPMs. Therefore, even if high channel-density ASIC readout chips are available, it is of interest to employ multiplexing readouts to allow multiple SiPMs sharing one readout channel [23]–[26]. Alternatively, one may reduce the number of SiPMs by light multiplexing in which one SiPM receives light outputs from multiple scintillators [27]. Unfortunately, both electronic and light multiplexing compromise timing. As a result, highly multiplexing readouts that are favorable for reducing detector complexity typically cannot support TOF detection [28].

We previously proposed and studied a stripline (SL) based highly multiplexing electronic readout that can maintain timing properties [29]. In this work, as depicted by the schematics

This work was supported in part by the National Research and Development Program for Major Research Instruments of Natural Science Foundation of China (Grant No. 62027808, 61927801) and the Sino-German Mobility Programme (Grant No. M-0387), and in part by the University of Chicago Radiology Seed Grant, the University of Chicago Comprehensive Cancer Center Program Pilot Grant and Team Award, the NIH R03 EB027343, and the NIH R01 EB029948.

F. Wang (wangfei123@hust.edu.cn), Q. Xie (qgxie@hust.edu.cn), and L. Liu are with the College of Life Science and Technology, Huazhong University of Science and Technology, Wuhan, China.

C.-M. Kao (c-kao@uchicago.edu) and H. Kim (heejongkim@uchicago.edu) are with The University of Chicago, Chicago, Illinois, USA.

X. Zhang is with the Wuhan National Laboratory for Optoelectronics, Huazhong University of Science and Technology, Wuhan, China

Y. Hua is with the Raycan Technology Co., Suzhou, China.

W.-S. Choong (wschoong@lbl.gov) is with the Lawrence Berkeley National Laboratory, Berkeley, California, USA.

Q. Xie is the correspondence author.

shown in Fig. 1(a) and explained below, we propose to employ this method for row- and column-wise electronic readout of an $N \times N$ array detector employing double-ended light readout in such a way that the front-end and back-end SiPM arrays were each read by a single SL. As a result, the array detector produces four outputs, yielding a multiplexing ratio of $N^2/2$.

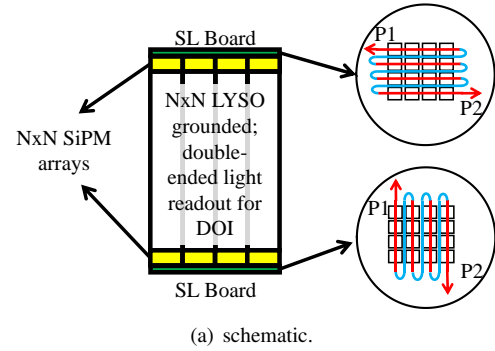
The objective of this work is to experimentally evaluate the proposed DOI and TOF-capable PET detector having significantly reduced electronic complexity. In Sect. II, we describe the designs of two detector modules (DM) that contain 4×4 and 8×8 scintillators. In Sect. III, we report the performance properties measured for these DMs. In Sect. IV, we provide concluding remarks and discuss the possible cause for the degradation in CRT observed with the 8×8 DM.

II. METHODS

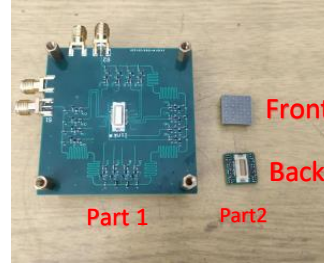
As shown in Figs. 1(b)&1(c), two DMs employing $3.0 \times 3.0 \times 20$ mm³ LYSO crystals were developed. Based on previous experiments in which we examined the dependence of the DOI resolution of a single LYSO crystal with various surface treatments [30], the four side surfaces of the crystals in these modules were grounded by using $9 \mu\text{m}$ grains. To minimize the escape of scintillation lights through them, these surfaces were then covered by approximately 0.2 mm thickness BaSO₄, yielding a crystal pitch of about 3.2 mm. On the other hand, the front and back surfaces of the crystals were polished and optically coupled to SiPM pixels by using optical grease. The Hamamatsu Multi-Pixel Photon Counter (MPPC) arrays S14161-3050HS were used. SiPM pixels in these arrays had an active detection area of 3.0 mm and a pitch of 3.2 mm, matching those of the crystals. Their breakdown voltages were 39 V. The bias voltages employed for the 4×4 and 8×8 DMs were, respectively, 46 V and 44 V because in preliminary experiments they were observed to yield signals having better quality over other voltages.

The design and principle of the SL readout have been previously described by us in [29], [31]. In short, the differential time of the signals arriving at the two ends of an SL, called the *SL differential time* δt , gives the position of the signal-producing SiPM on the SL. The SL readout is simple and can be made highly compact because it uses only a small amount of passive electronics [32]. In our previous works, serpentine SL segments were used between every two SiPMs to increase the discriminability of individual SiPMs on an SL. In this work, to decrease the number of positions needed for discrimination, hence further reducing the electronic complexity, serpentine segments (depicted by the blue segment in Fig. 1(a)) were introduced only between rows or columns to allow discrimination of the row or column position of the signal-producing crystal. For these DMs, the SL length between adjacent rows (or columns) was 13 cm, which corresponded to a propagation delay of approximately 1 ns.

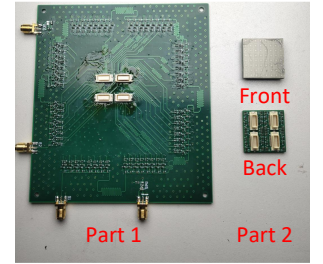
A Na-22 source was used for all measurements. For position and energy measurements, the source was placed at 2 cm in front of the DM and single events were collected. For CRT and DOI measurements, coincidence events between a



(a) schematic.



(b) 4×4 DM.



(c) 8×8 DM.

Figure 1: (a) A schematic showing the design of the array detector and the electronic readout that uses a single SL for reading a SiPM array. Each SL has two outputs and therefore the detector has four outputs. The SL segments in blue do not receive signals but provide propagation delay to encode the row or column position of the signal-producing crystal. (b) A photo of the 4×4 DM, showing the SL board for the front-end SiPM array (part 1), and the front and back sides of the SiPM array (part 2). (c) A photo of the 8×8 DM that similarly shows the SL board and the SiPM array. To allow easy replacement of electronic parts, the SLs of these DMs are loosely laid out on the circuit boards. They can be made much more compact to potentially allow the development of 4-side tileable DMs.

reference detector and the DM were acquired. The reference detector consisted of a single $2 \times 2 \times 20$ mm³ LYSO coupled to a SensL FC30035 SiPM. The CRT of the reference detector was measured to be 302 ps. For DOI measurement, the reference detector was used to electronically collimate the annihilation-photon beam from the Na-22 source. A linear stage was used to move the collimated beam to hit the DM from the side at a number of DOI positions, ranging from 3 mm to 17 mm. Outputs of the DM and reference detector were sampled at 2 GHz by using DRS4 evaluation boards [33], [34] and saved.

The saved waveform data were processed to yield relevant event information. In short, δt was computed for the front-end (back-end) SL for discriminating the row (column) position of the signal-producing crystal. The front-end (back-end) pulse height (PH), denoted by F (B), was the sum of the waveform samples of the two signals observed at the outputs of the front-end (back-end) SLs. The event PH, denoted by E , and the DOI ratio, denoted by α , were computed as $E = F + B$ and $\alpha = F/(F + B)$. The coincidence differential time, Δt , was the time difference between when signals were detected by the front-end SL of the DM and by the reference detector. For measuring δt and Δt , the occurrence time of a signal was determined by using constant fraction discrimination (CFD)

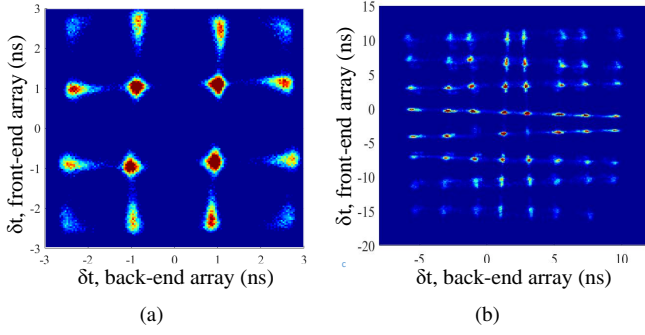


Figure 2: 2d histograms of front-end δt vs back-end δt obtained for the 4×4 (a) and 8×8 (b) DMs.

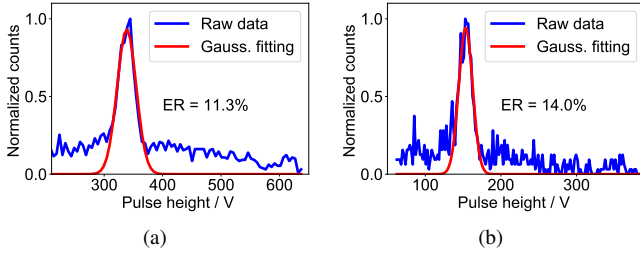


Figure 3: Sample crystal-level PHS obtained for the 4×4 (a) and 8×8 (b) DMs.

that was digitally implemented. The CFD threshold was varied for identifying the value that produced the best δt and Δt resolutions, which were then reported.

III. RESULTS

A. Position discrimination and energy resolution

Figure 2 shows the 2d histograms of the SL differential times δt obtained for the two DMs. Overall, all crystals in both DMs were well discriminated. For the 8×8 DM in Fig. 2(b), the crystal at the lower-right corner was absent and the crystal in the fifth row and third column was weak. We believed that they were a result of loose electronic contacts. It is also observed that the rows (columns) are not perfectly horizontal (vertical) but have a small slope. This slope, which is more evident with the 8×8 DM, is due to the nonzero SL length between adjacent SiPMs in the same row (column). To convert a measured front-end (back-end) δt value to a row (column) number, we identified the N largest peaks in the 1d histogram of front-end (back-end) δt and used the midpoints of these peaks to obtain the boundaries for defining N rows (columns). The pulse-height spectrum (PHS) for a crystal in a DM was then obtained by histogramming events that were assigned to that crystal by using these boundaries. Figure 3 shows sample PHS obtained for the two DMs, showing that the photopeak could be readily identified. By fitting the photopeak with a Gaussian, the ER of a crystal was reported as the percentage ratio of the width of the Gaussian in FWHM to its center position. For the 4×4 DM, as shown in Fig. 4, the crystal-level ER ranged from 11.3% to 19.3%, with the majority in 10%-15% and an average value of 14.1%. For the 8×8 DM, as

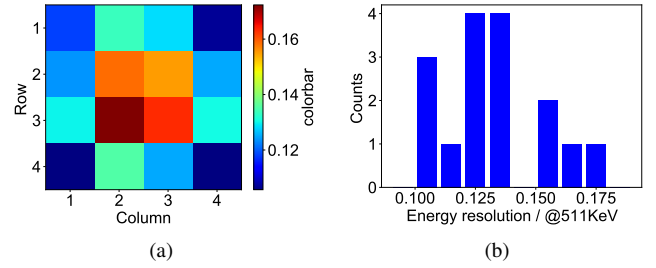


Figure 4: A map showing the ERs obtained for individual crystals of the 4×4 DM (a) and the histogram showing its distribution (b).

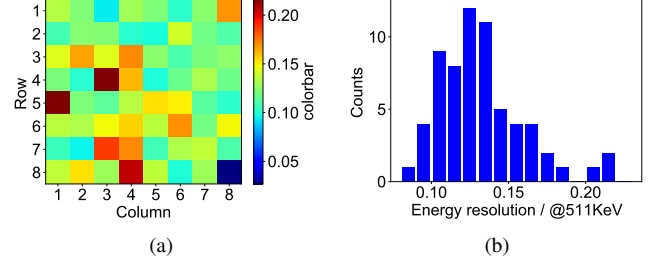


Figure 5: A map showing the ERs obtained for individual crystals of the 8×8 DM (a) and the histogram showing its distribution (b).

shown in Fig. 5, its ER ranged from 9.5% to 21.6%, with the majority in 10%-17% and an average value of 13.9%. These values are consistent with the ERs reported in the literature for LYSO-based detectors. The crystal-level ER did not show noticeable degradation when the array size of the DM was increased from 4×4 to 8×8 . Generally speaking, crystals close to the edges had better ERs.

B. DOI and TOF Resolutions

Figure 6(a) shows the histograms of the DOI ratio α obtained for the 4×4 DM at six DOI positions, including 3 mm, 5 mm, 9 mm, 13 mm, 15 mm, and 17 mm (the overall length of the crystal was 20 mm). As shown, the centroid position of these histograms decreased as the DOI position increased. In Fig. 6(b), the blue curve and its error bars show, respectively, the variations of the centroid position and FWHM width (obtained by Gaussian fit) of these histograms with their DOI position. The curve shows that the centroid position of the DOI-ratio decreased linearly with the DOI position. By linearly interpolating the measured data points on the blue curve, we obtained a calibration curve for converting DOI ratio to *measured DOI*. Using this curve, the FWHMs of the DOI-ratio histograms were accordingly converted to the resolutions of the measured DOIs. The orange curve in Fig. 6(b) and its error bars are the resulting calibration curve and DOI resolutions. The average of the DOI resolutions obtained at DOI positions ranging from 3 mm to 17 mm was 2.5 mm. Figures 6(c) and 6(d) similarly show the results obtained for the 8×8 DM. The variation of the centroid of the DOI-ratio histogram with the DOI position departed slightly from linearity at positions close to the ends of the crystal (3 mm and 17 mm DOIs) but overall it remained highly linear. The

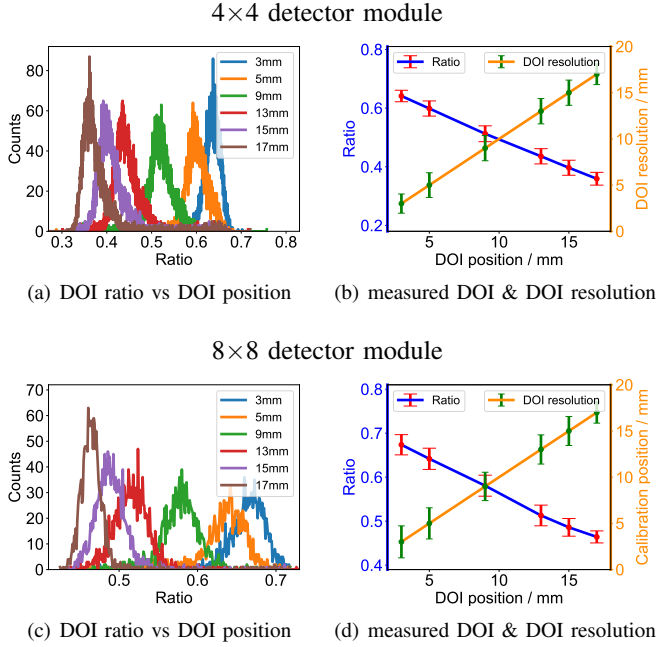


Figure 6: (a) Histograms of the DOI ratio obtained for the 4×4 DM at six DOI positions ranging from 3 mm to 17 mm. (b) The blue curve plots the centroid positions of the DOI-ratio histograms versus their DOI positions, with the error bars showing the FWHMs of the histograms. The orange curve shows the measured versus actual DOI positions, with the error bars indicating the DOI resolutions. Likewise, (c) and (d) are the results equivalent to (a) and (b) obtained for the 8×8 DM. See text for detail.

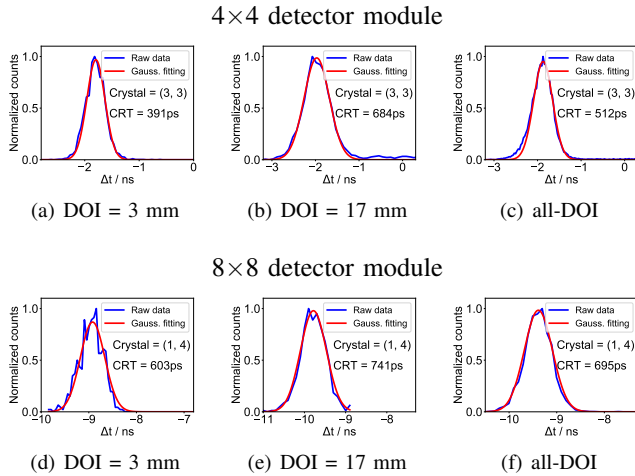


Figure 7: The best-CRT histograms of Δt (blue curves) and their Gaussian fits (red curves) obtained for the 4×4 (top) and 8×8 (bottom) DMs for events at DOI = 3 mm (first column), for events at DOI = 17 mm (2nd column), and for all events (3rd column). The (row, column) crystal positions where these CRTs were obtained and the FWHMs of the Gaussian fits are also shown.

average DOI resolution was 3.1 mm, slightly inferior to that of the 4×4 DM. For clinical imaging, a DOI resolution of 3-4 mm is adequate.

For CRT measurement, we obtained histograms of the coincidence differential time Δt between every crystals of the DM and the reference detector when the latter was positioned

to direct collimated beams to various DOI positions. We then applied Gaussian fits to the resulting histograms and the FWHMs of the Gaussian were reported as the CRT. At each DOI position, we identified the best CRT obtained among all crystals of a DM. We also similarly obtained the best CRT by using all acquired events, disregarding the DOI positions (called *all-DOI* CRT below). The first and second columns in Fig. 7 show, respectively, the histograms and CRTs of the best CRT results obtained at DOI = 3 mm and 17 mm. The third column shows the histograms and CRTs of the best all-DOI CRT results. The top and bottom rows show the results for the 4×4 and 8×8 DMs, respectively. Generally, as the DOI increased the CRT histogram became wider and the centroid position shifted. For the 4×4 DM, we obtained 391 ps best CRT at DOI = 3 mm, 684 ps best CRT at DOI = 17 mm, and 512 ps best all-DOI CRT. For the 8×8 DM, these figures became 603 ps, 741 ps, and 695 ps, respectively. We observe that, as previously reported by others [35], [36], in general, CRT degraded as DOI increased. Also, CRT degraded considerably when the DM array size was increased from 4×4 to 8×8 . It is noted that the all-DOI CRT was obtained by using approximately the same number of detected events at all measured DOI positions. In actual imaging, CRTs at larger DOIs have smaller contributions to the overall CRT because there are fewer events at larger DOIs. Therefore, the non-DOI CRT will be smaller than the all-DOI CRT reported above.

IV. CONCLUSION AND DISCUSSION

In this work, we investigate the concept of using a highly multiplexing SL-based readout for DOI- and TOF-capable PET array detectors that consist of $N \times N$ pixellated scintillators with double-ended light readouts by developing 4×4 and 8×8 DMs that employ $3.0 \times 3.0 \times 20$ mm³ LYSO crystals and measuring their detection performance properties. For both DMs, our results show that all but one crystal (possibly due to loose electric contact) is discriminated, the average crystal-level ER is better than 15%, and the average DOI resolution is better than 3.5 mm. When the array size of the DM is increased from 4×4 to 8×8 , the ER and DOI resolution deteriorate only slightly. In coincidence detection with a single-pixel reference detector, generally, better CRTs are obtained at smaller DOIs. However, the CRT degrades considerably as the array size is increased. For example, at DOI = 3 mm (17 mm), the best CRTs are 391 ps and 684 ps (603 ps and 741 ps) for the 4×4 and 8×8 DMs, respectively. Thus, further improvement in the CRT is desired, especially for larger arrays.

A plausible reason for the degradation of CRT when the array size increases is given below. The proposed readout assumes that, at any instant, of all the SiPMs sharing an SL only the one that is coupled to the scintillator with which a gamma ray first interacts produces a signal pulse (called the *real pulse* below). If additional pulses occur in different rows (or columns), the observed signal at an output of the SL is the sum of the real pulse and these additional pulses that are delayed by different amounts. The arrival time derived from the summed pulse can be different from the arrival time of the real pulse, hence degraded CRT, if the additional pulses have

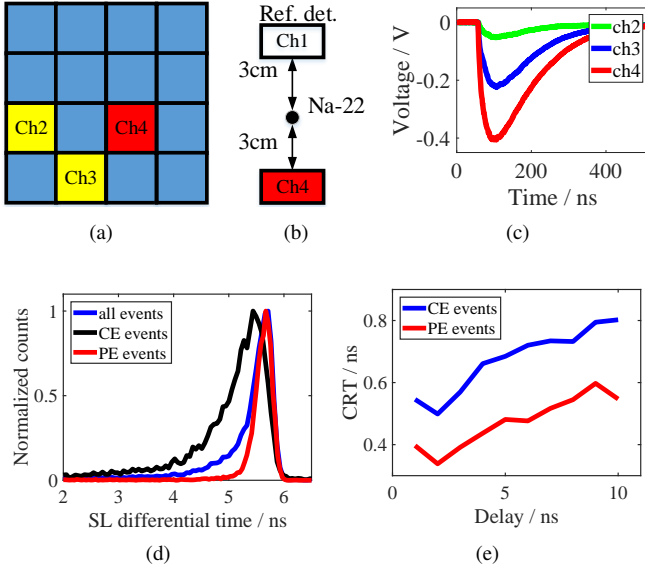


Figure 8: (a) A DRS4 evaluation board was used to acquire the outputs of three SiPMs in a 4×4 array, marked by ch2-ch4, and a single-pixel reference detector (ch1, not shown). (b) A Na-22 source was placed at 3 cm above the ch4 SiPM and the reference detector was used to electronically collimate the gamma rays onto the ch4 SiPM. (c) Sample ch2-ch4 signals that were acquired when ch1 and ch4 were triggered in coincidence. (d) Normalized δt histograms derived from synthesized signals by using all events, CE events, and PE events. (e) The variation of the CRT derived from synthesized signals with the propagation delay between rows. See text for details.

non-negligible amplitudes. To test this hypothesis, we used a 4×4 array of LYSOs with single-ended light readout by using SiPMs. The crystal array, including the surface treatment, and the SiPM array used were identical to those used in the 4×4 DM. However, the SiPM outputs were not merged by an SL. As depicted in Figs. 8(a)&8(b), the outputs of three SiPMs of the array (ch2-ch4) and the single-pixel reference detector (ch1), were acquired by using a DRS4 evaluation board when ch1 and ch4 were both triggered. The reference detector was used to electronically collimate the annihilation photons from a Na-22 source onto the ch4 SiPM. Figure 8(c) shows that however ch2 and ch3 SiPMs could produce substantial signals.

To examine how the additional pulses may affect event positioning and CRT, we synthesized SL output signals by summing delayed ch2-ch3 signals by assuming that the array was read by an SL with a 6 ns propagation delay between rows. Figure 8(d) shows the normalized δt histograms derived from the synthesized signals by applying leading-edge discrimination (LED) with a -30 mV threshold for time pickup, by using all the acquired events (blue curve) and by using the photopeak-energy (PE) and Compton-energy (CE) events (red and black curves respectively). The PE and CE events were those whose ch4 signal¹ had an energy in 460-600 keV and <460 keV, respectively. Consistent with the expectations that events undergoing photoelectric interaction produce signals only at ch4 and events undergoing Compton interactions can

produce signals at ch2 or ch3 also, the red curve is best localizing (narrowest) and the blue curve is least localizing (widest). Figure 8(e) shows how the CRTs derived from the synthesized pulses vary with the between-row delay. It is observed that the CRT generally degraded as the delay increased, and that the CRT of the CE events was substantially worse than that of the PE events. The former suggests that, for best CRT, we shall use the smallest delay between rows or columns that is sufficient for discriminating rows or columns. The latter indicates that the CRT can be substantially deteriorated when multiple signals are injected into an SL in an event.

The additional pulses can be due to escape of scintillation lights through BaSO₄ into neighboring crystals, diffusion of scintillation lights at the interface of the LYSO and SiPM arrays, and Compton scattering of annihilation photons within the array detector. Based on the substantial signal amplitude observed in ch2 and ch4, we believe that in our case intra-detector Compton scattering is the main cause. This issue, and solutions to mitigate its effects, need to be further investigated in future studies.

REFERENCES

- [1] C. Kim, D. McDaniel, and A. Ganin, "Time-of-flight PET detector based on multi-pixel photon counter and its challenges," *IEEE Trans. Nucl. Sci.*, vol. 58, pp. 3–8, 2011.
- [2] T. Lewellen, "Recent developments in PET detector technology," *Phys. Med. Biol.*, vol. 53, p. R287, 2008.
- [3] P. Lecoq, "Pushing the limits in time-of-flight PET imaging," *IEEE Trans. Radiat. Plasma Med. Sci.*, vol. 1, pp. 473–485, 2017.
- [4] J. Thiessen *et al.*, "Performance evaluation of SensL SiPM arrays for high-resolution PET," in *IEEE NSS/MIC Conference Record*, 2013, pp. 1–4.
- [5] T. Zhao *et al.*, "Feasibility of high-resolution PET detector readout by 2-D tetra-lateral position-sensitive silicon photomultiplier," *IEEE Trans. Radiat. Plasma Med. Sci.*, vol. 3, pp. 621–625, 2019.
- [6] E. Venialgo *et al.*, "Toward a full-flexible and fast-prototyping TOF-PET block detector based on TDC-on-FPGA," *IEEE Trans. Radiat. Plasma Med. Sci.*, vol. 3, pp. 538–548, 2019.
- [7] P. Lecoq and S. Gundacker, "SiPM applications in positron emission tomography: toward ultimate PET time-of-flight resolution," *Eur. Phys. J. Plus*, vol. 136, pp. 1–16, 2021.
- [8] D. Schaart *et al.*, "LaBr(3):Ce and SiPMs for time-of-flight PET: achieving 100 ps coincidence resolving time," *Phys. Med. Biol.*, vol. 55, pp. N179–89, 2010.
- [9] S. Gundacker *et al.*, "State of the art timing in TOF-PET detectors with LuAG, GAGG and L(Y)SO scintillators of various sizes coupled to FBK-SiPMs," *J. Instrum.*, vol. 11, p. P08008, 2016.
- [10] M. Nemallapudi *et al.*, "Sub-100 ps coincidence time resolution for positron emission tomography with LSO:Ce codoped with Ca," *Phys. Med. Biol.*, vol. 60, pp. 4635–4649, 2015.

¹The translation factor for converting PH to energy was derived based the PHs of the summed signals.

- [11] S. Gundacker *et al.*, “Time of flight positron emission tomography towards 100ps resolution with L(Y)SO: an experimental and theoretical analysis,” *J. Instrum.*, vol. 8, p. P07014, 2013.
- [12] J. Cates, R. Vinke, and C. Levin, “Analytical calculation of the lower bound on timing resolution for PET scintillation detectors comprising high-aspect-ratio crystal elements,” *Phys. Med. Biol.*, vol. 60, pp. 5141–5161, 2015.
- [13] H. Kang *et al.*, “A dual-ended readout detector using a meantime method for SiPM TOF-DOI PET,” *IEEE Trans. Nucl. Sci.*, vol. 62, pp. 1935–1943, 2015.
- [14] N. Inadama *et al.*, “Development of a DOI PET detector having the structure of the X’tal cube extended in one direction,” *IEEE Trans. Nucl. Sci.*, vol. 63, pp. 2509–2516, 2016.
- [15] J. Yeom *et al.*, “Comparison of end/side scintillator readout with digital-SiPM for ToF PET,” in *IEEE NSS/MIC Conference Record*, 2013, pp. 1–3.
- [16] F. Nishikido *et al.*, “Four-layer DOI-PET detector with a silicon photomultiplier array,” in *IEEE NSS/MIC Conference Record*, 2008, pp. 3923–3925.
- [17] M. Ito, S. Hong, and J. Lee, “Positron emission tomography (PET) detectors with depth-of-interaction (DOI) capability,” *Biomed. Eng. Lett.*, vol. 1, pp. 70–81, 2011.
- [18] K. Champley *et al.*, “Statistical LOR estimation for a high-resolution dMiCE PET detector,” *Phys. Med. Biol.*, vol. 54, pp. 6369–6382, 2009.
- [19] G. Prenosil *et al.*, “Performance characteristics of the Biograph Vision Quadra PET/CT system with a long axial field of view using the NEMA NU 2-2018 standard,” *J. Nucl. Med.*, vol. 63, pp. 476–484, 2022.
- [20] C. Levin *et al.*, “Design features and mutual compatibility studies of the time-of-flight PET capable GE SIGNA PET/MR system,” *IEEE Trans. Med. Imag.*, vol. 35, pp. 1907–1914, 2016.
- [21] I. Rausch *et al.*, “Performance evaluation of the Vereos PET/CT system according to the NEMA NU2-2012 standard,” *J. Nucl. Med.*, vol. 60, pp. 561–567, 2019.
- [22] B. Spencer *et al.*, “Performance evaluation of the uEXPLORER total-body PET/CT scanner based on NEMA NU 2-2018 with additional tests to characterize PET scanners with a long axial field of view,” *J. Nucl. Med.*, vol. 62, pp. 861–870, 2021.
- [23] H. Park and J. Lee, “Highly multiplexed SiPM signal readout for brain-dedicated TOF-DOI PET detectors,” *Physica Medica*, vol. 68, pp. 117–123, 2019.
- [24] E. Downie, X. Yang, and H. Peng, “Investigation of analog charge multiplexing schemes for SiPM based PET block detectors,” *Phys. Med. Biol.*, vol. 58, p. 3943, 2013.
- [25] A. Goertzen *et al.*, “Design and performance of a resistor multiplexing readout circuit for a SiPM detector,” *IEEE Trans. Nucl. Sci.*, vol. 60, pp. 1541–1549, 2013.
- [26] M. Bieniosek *et al.*, “Analog filtering methods improve leading edge timing performance of multiplexed SiPMs,” *Phys. Med. Biol.*, vol. 61, p. N427, 2016.
- [27] Y. Eiji *et al.*, “Gapless implementation of crosshair light-sharing PET detector,” *Nucl. Instrum. Methods Phys. Res. A*, vol. 1021, p. 165922, 2022.
- [28] Z. Kuang *et al.*, “Dual-ended readout small animal PET detector by using 0.5 mm pixelated LYSO crystal arrays and SiPMs,” *Nucl. Instrum. Methods Phys. Res. A*, vol. 917, pp. 1–8, 2019.
- [29] H. Kim *et al.*, “Multiplexing readout for time-of-flight (TOF) PET detectors Using striplines,” *IEEE Trans. Radiat. Plasma Med. Sci.*, vol. 5, pp. 662–670, 2021.
- [30] C. Tian, “DOI-PET detector with multiplexing readout,” Master’s thesis, Huazhong University of Science and Technology, 2020.
- [31] F. Wang *et al.*, “DOI- and TOF-capable PET array detector using double-ended light readout and stripline-based row and column electronic readout,” in *IEEE NSS/MIC Conference Record*, 2021, pp. 1–4.
- [32] H. Kim *et al.*, “Development of a PET/EPRI combined imaging system for assessing tumor hypoxia,” *J. Instrum.*, vol. 16, p. P03031, 2021.
- [33] S. Ritt, “Design and performance of the 6 GHz waveform digitizing chip DRS4,” in *IEEE NSS/MIC Conference Record*, 2008, pp. 1512–1515.
- [34] M. Bitossi, R. Paoletti, and D. Tescaro, “Ultra-fast sampling and data acquisition using the DRS4 waveform digitizer,” *IEEE Trans. Nucl. Sci.*, vol. 63, pp. 2309–2316, 2016.
- [35] R. Vinke *et al.*, “The lower timing resolution bound for scintillators with non-negligible optical photon transport time in time-of-flight PET,” *Phys. Med. Biol.*, vol. 59, p. 6215, sep 2014.
- [36] R. Wiener *et al.*, “Signal analysis for improved timing resolution with scintillation detectors for TOF PET imaging,” in *IEEE NSS/MIC Conference Record*, 2010, pp. 1991–1995.